How well does the Rayleigh model describe the E-vector distribution of skylight in clear and cloudy conditions? A full-sky polarimetric study

Bence Suhai and Gábor Horváth

Biooptics Laboratory, Department of Biological Physics, Loránd Eötvös University, H-1117 Budapest, Pázmány sétány 1, Hungary

Received December 18, 2003; revised manuscript received April 5, 2004; accepted April 28, 2004

We present the first high-resolution maps of Rayleigh behavior in clear and cloudy sky conditions measured by full-sky imaging polarimetry at the wavelengths of 650 nm (red), 550 nm (green), and 450 nm (blue) versus the solar elevation angle θ_s. Our maps display those celestial areas at which the deviation $\Delta\alpha = |\alpha_{\text{meas}} - \alpha_{\text{Rayleigh}}|$ is below the threshold $\alpha_{\text{thres}} = 5°$, where α_{meas} is the angle of polarization of skylight measured by full-sky imaging polarimetry, and α_{Rayleigh} is the celestial angle of polarization calculated on the basis of the single-scattering Rayleigh model. From these maps we derived the proportion r of the full sky for which the single-scattering Rayleigh model describes well (with an accuracy of $\Delta\alpha = 5°$) the E-vector alignment of skylight. Depending on θ_s, r is high for clear skies, especially for low solar elevations ($40\% < r < 70\%$ for $\theta_s \leqslant 13°$). Depending on the cloud cover and the solar illumination, r decreases more or less under cloudy conditions, but sometimes its value remains remarkably high, especially at low solar elevations ($r_{\text{max}} = 69\%$ for $\theta_s = 0°$). The proportion r of the sky that follows the Rayleigh model is usually higher for shorter wavelengths under clear as well as cloudy sky conditions. This partly explains why the shorter wavelengths are generally preferred by animals navigating by means of the celestial polarization. We found that the celestial E-vector pattern generally follows the Rayleigh pattern well, which is a fundamental hypothesis in the studies of animal orientation and human navigation (e.g., in aircraft flying near the geomagnetic poles and using a polarization sky compass) with the use of the celestial α pattern.

OCIS codes: 010.3920, 100.0100, 120.5410, 260.5430, 280.0280, 290.1310.

1. INTRODUCTION

Many animals are sensitive to the linear polarization of light, and several species can orient by means of the celestial polarization pattern.[1] These animals use the distribution of the electric field vector (E vector) of skylight in the ultraviolet, blue, or green part of the spectrum.[2] In the models and theories explaining the orientation behavior of these animals, it is always assumed that in any point of the celestial hemisphere the E vector of skylight is perpendicular to the scattering plane, i.e., the plane through the sun, the observer, and the point observed.[3–22] In other words, in the literature dealing with the sky-compass orientation of these animals it is hypothesized that the celestial E-vector pattern follows the rules of the primary Rayleigh scattering of sunlight in the atmosphere. This hypothesis originates from Karl von Frisch,[23] who supposed that this condition is realized for most areas of the clear sky when he tried to interpret his pioneering observations on the celestial orientation of honeybees. Hence for these studies it is important to know how the celestial E-vector pattern follows the rules of primary Rayleigh scattering.

A widespread belief is that the Vikings were able to navigate on the open sea by means of the E-vector direction of clear (blue) patches of the sky when the sun was occluded by clouds. It is hypothesized[24–27] that under partly cloudy conditions, a Viking navigator could locate the sun if he knew that the solar direction is perpendicular to the E vector of skylight determined by a mysterious birefringent crystal called "sunstone." A similar celestial polarimetric method was used in aircraft flying in the vicinity of the geomagnetic poles.[25] Obviously, such a navigation is practicable only if the single-scattering Rayleigh predictions are correct for the sky. Even small E-vector deviations can produce large errors if used in a strictly geometrical way to locate the sun, impairing the navigator's ability to reach his actual goal. Hence in considering how accurately a navigator could orient by this method, we must look also at how the E-vector pattern of real skies differs from the single-scattering Rayleigh pattern.

Although there are some studies of how the celestial E-vector pattern follows the Rayleigh pattern,[28,29] these investigations are restricted to relatively small numbers of points in the sky, owing to the use of scanning point-source polarimeters. Only the technique of full-sky imaging polarimetry[30–33] made it possible to determine the map of the Rayleigh behavior of the E-vector direction in real skies. Such a map displays those celestial areas at which the deviation $\Delta\alpha = |\alpha_{\text{meas}} - \alpha_{\text{Rayleigh}}|$ is below an arbitrary threshold, where α_{meas} is the angle of polarization of skylight measured by full-sky-imaging polarimetry, and α_{Rayleigh} is the angle of polarization of skylight calculated on the basis of the single-scattering Rayleigh model. The aim of this work is to present the first high-resolution maps of Rayleigh behavior in clear and cloudy sky conditions measured by full-sky imaging polarimetry in the red (650 nm), green (550 nm), and blue (450 nm)

1084-7529/2004/091669-08$15.00

spectral ranges versus the solar elevation angle θ_s. From these maps we derived the proportion r of the sky for which the single-scattering Rayleigh model describes well the E-vector alignment of skylight.

2. MATERIALS AND METHODS

In this work we used the α patterns (the angle of polarization α is measured clockwise from the local meridian) measured for clear and cloudy skies and presented earlier by Pomozi *et al.*[34] These patterns were measured by full-sky imaging polarimetry in Tunisia at wavelengths of 650 nm (red), 550 nm (green), and 450 nm (blue). For the clear and cloudy sky series, the solar elevation angles θ_s were approximately the same (see column θ_s in Tables 1–3 below). After an appropriate rotation of a given pattern of the cloudy sky series around the zenith, the solar azimuth angle becomes the same as that for the corre-

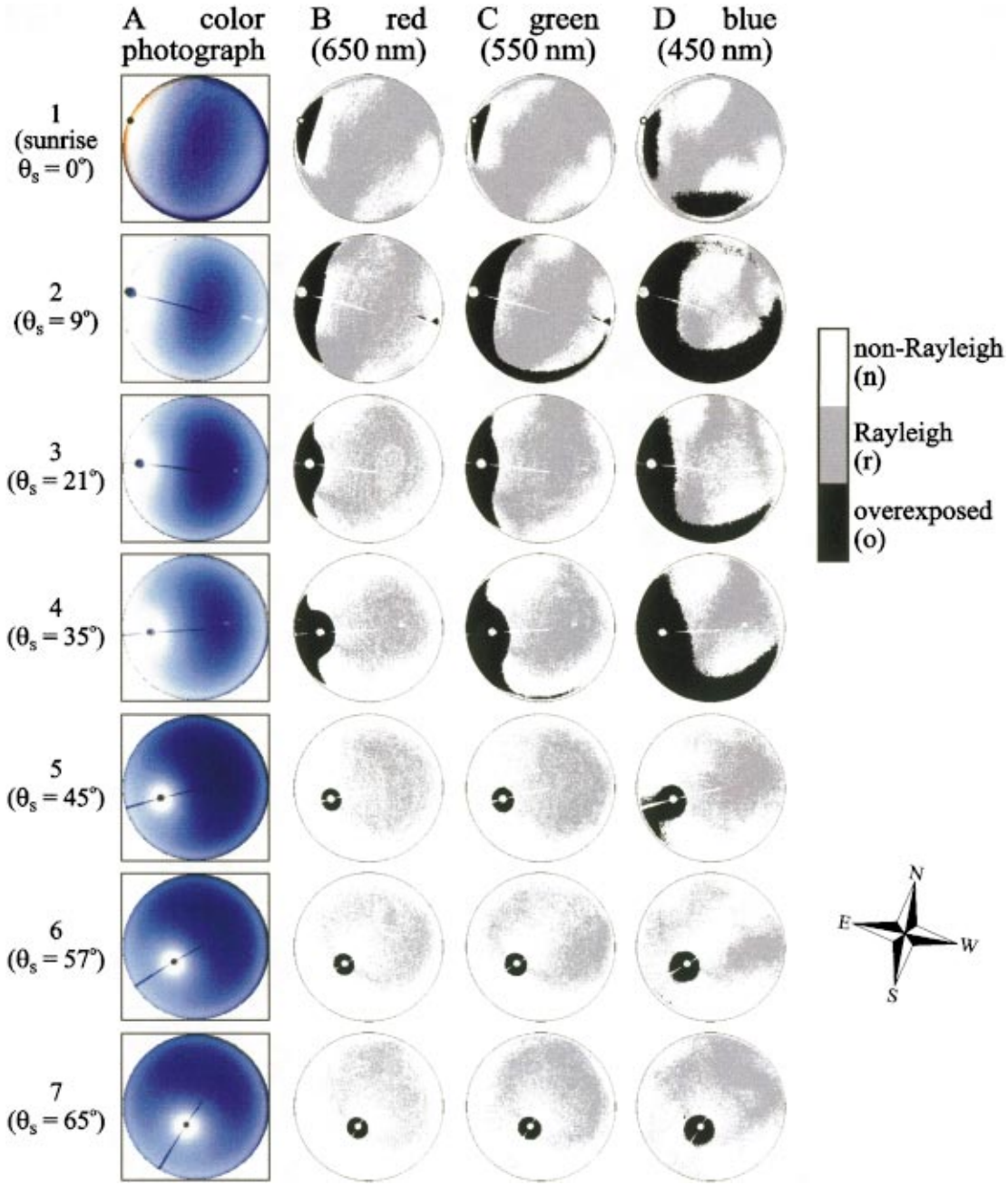

Fig. 1. A, Distribution of the total radiance of clear skies versus the solar elevation angle θ_s from the horizon. The center of the circular pictures is the zenith, the perimeter is the horizon, and the zenith angle ϕ is proportional to the radius ($\phi_{\text{zenith}} = 0°$, $\phi_{\text{horizon}} = 90°$). B, C, D, Maps of the proportion r of the sky that follows the Rayleigh model for clear skies at the wavelengths 650 nm (red), 550 nm (green), and 450 nm (blue) versus θ_s. "Rayleigh" points with $\Delta\alpha = |\alpha_{\text{meas}} - \alpha_{\text{Rayleigh}}| \leq 5°$ are shaded gray, "non-Rayleigh" points with $\Delta\alpha > 5°$ are white, and overexposed points are black. The approximately hourly positions of the sun are represented by dots or the disk of the sun occulter. The radial bar in the circular pictures is the wire of the sun occulter. The compass rose shows the geographic (true) compass directions. Note that east and west are transposed in the compass rose, because we are looking upward at the skydome rather than downward at a map. The numerical values of r, n, and o determined for these skies are shown in Table 1.

sponding pattern of the clear sky series. The clouds were detected algorithmically in the color pictures of the skies as described by Pomozi *et al.*[34]

The polarimeter and the evaluation procedure are described in detail by Gál *et al.*[32] About the calibrated instrumentation and evaluation procedures, we mention here only the following: An angle of view of 180° was ensured by using a fisheye lens (Nikon-Nikkor, *f*2.8, focal length 8 mm) including a built-in rotating disk mounted with three broadband (275–750 nm) neutral density linearly polarizing filters (HNP′B, Polaroid Corporation) with three different polarization axes (0°, 45°, and 90° from the radius of the disk). The detector was a photoemulsion (Fujichrome Sensia II ASA 100 color reversal film; the maxima and half-bandwidths of its spectral sensitivity curves were $\lambda_{red} = 650 \pm 30$ nm, $\lambda_{green} = 550 \pm 30$ nm, $\lambda_{blue} = 450 \pm 50$ nm) in a roll-film photographic camera (Nikon F801). From a given sky, three photographs were taken for the three different alignments of the transmission axis of the polarizers on the built-in rotating disk. The camera was set up on a tripod such that the optical axis of the fisheye lens was vertical. With a personal computer, after 8-bit digitization (by a Hewlett Packard ScanJet 6100C) and evaluation of the three developed color images for a given sky, the patterns of radiance and the degree and angle of polarization of skylight were determined as high-resolution, color-coded, two-dimensional circular maps. These patterns were ob-

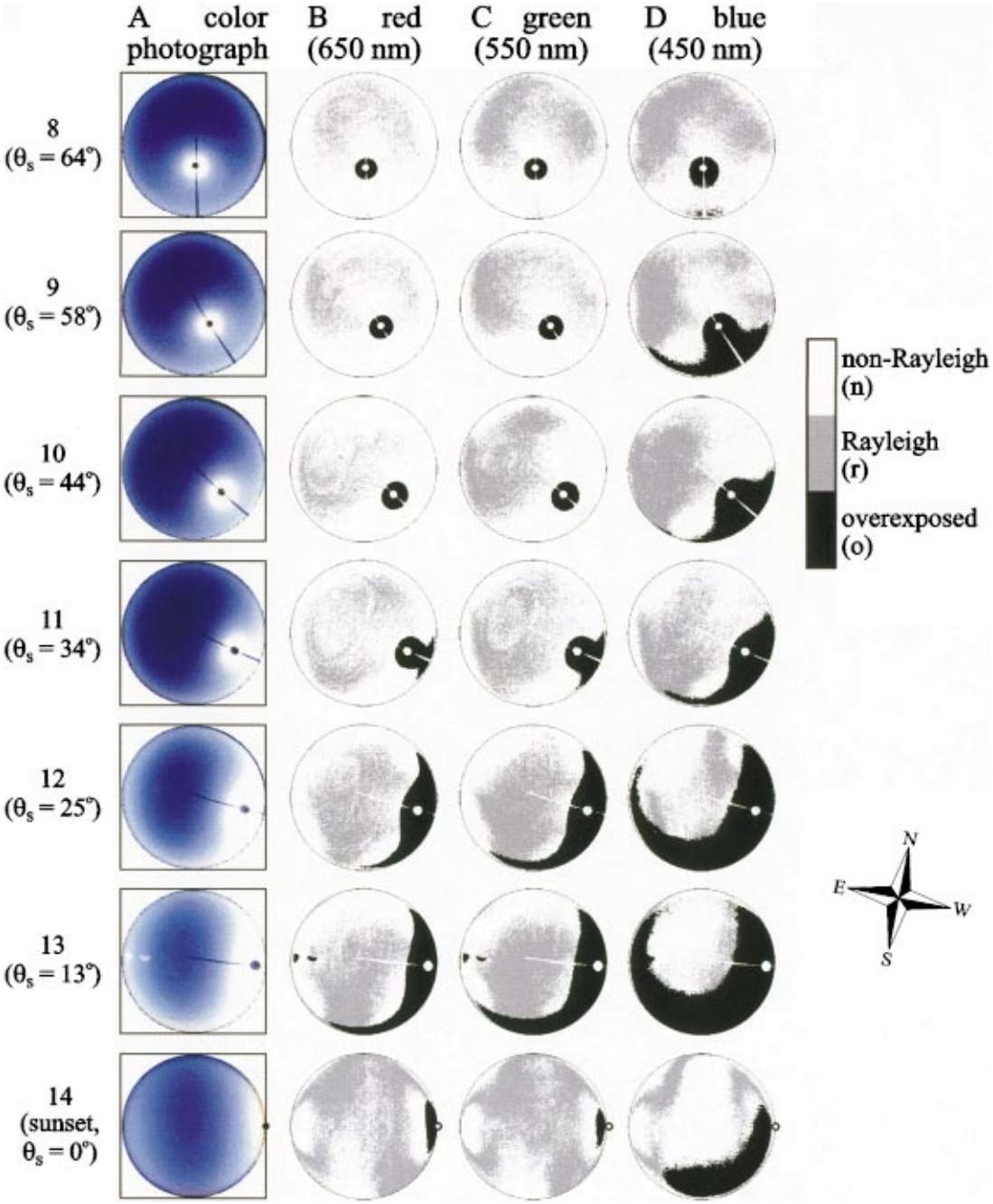

Fig. 1 (continued).

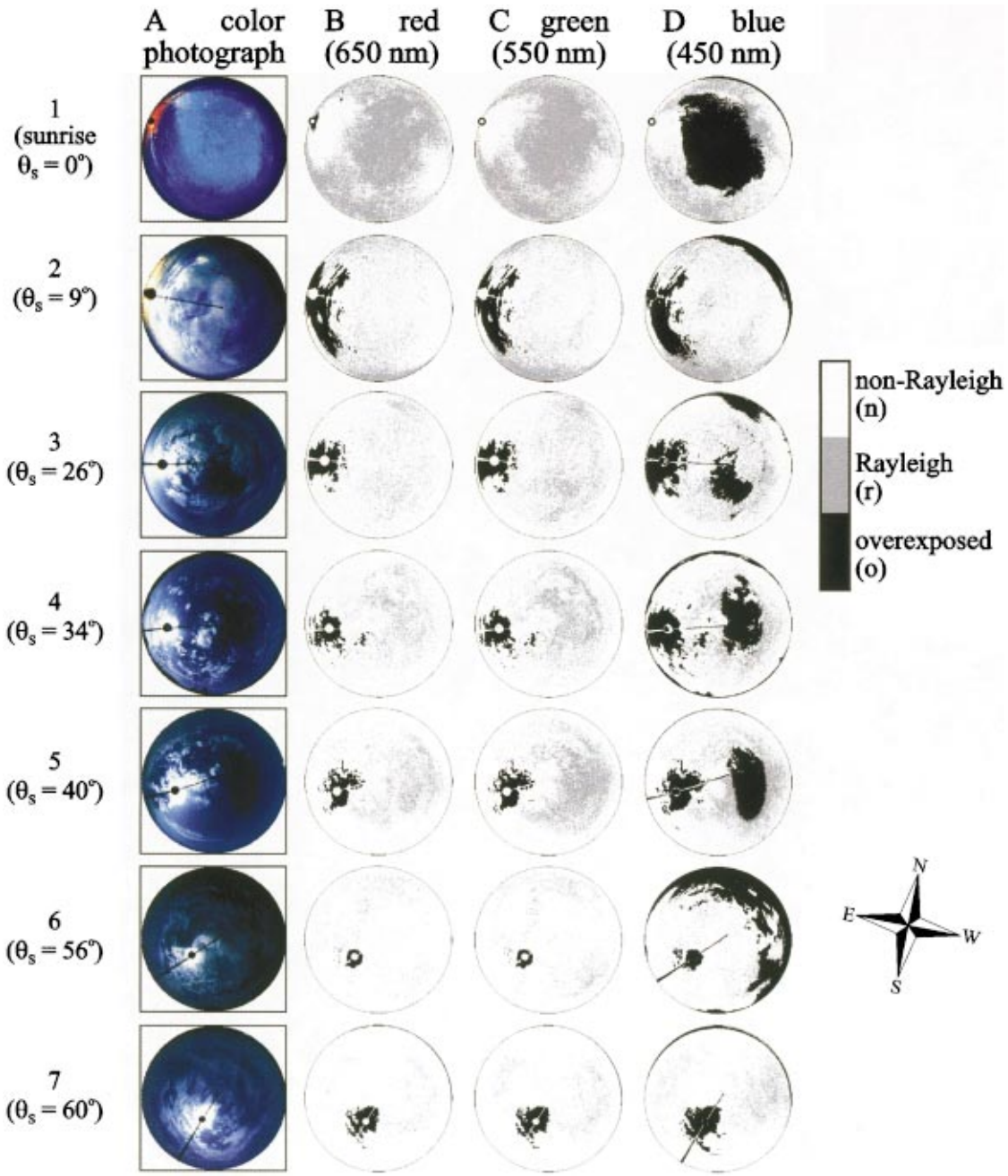

Fig. 2. As Fig. 1 but for partly cloudy skies, with approximately the same solar elevation angles θ_s and the same solar azimuth angles (due to appropriate rotations of the sky patterns around the zenith) as in Fig. 1. The numerical values of r, n, and o determined for these skies are shown in Tables 2 and 3.

tained in the red, green, and blue spectral ranges, in which the three color-sensitive layers of the photoemulsion used have maximal sensitivity. The red, green, and blue spectral ranges were obtained by using the scanner's digital image-processing program to separate the color channels in the digitized images.

The E-vector pattern of the Rayleigh sky at a given sun position was calculated on the basis of the single-scattering Rayleigh model[29]: In the single-scattering Rayleigh atmosphere the E-vector direction of skylight is perpendicular to the plane of scattering determined by the observer, the point observed, and the sun, independently of the wavelength.

Using the measured α pattern of the sky in a given spectral range and at a given sun position, we calculated the angle of polarization difference $\Delta\alpha = |\alpha_{\text{meas}} - \alpha_{\text{Rayleigh}}|$ at every celestial point between the real and single-scattering Rayleigh skies. Then the number N_{Rayleigh} of those celestial points was counted for which $\Delta\alpha \leqslant \alpha_{\text{thres}} = 5°$. We introduce the proportion r of the sky that follows the Rayleigh model, the definition of which is $r = N_{\text{Rayleigh}}/N$, where $N = 150\,000$ is the total number of pixels in the circular picture of the sky. [In Ref. 34 the number of pixels of the full sky was $N = 543\,000$. In this work we performed an aggregation of pixels in order to hasten the calculation of the celestial

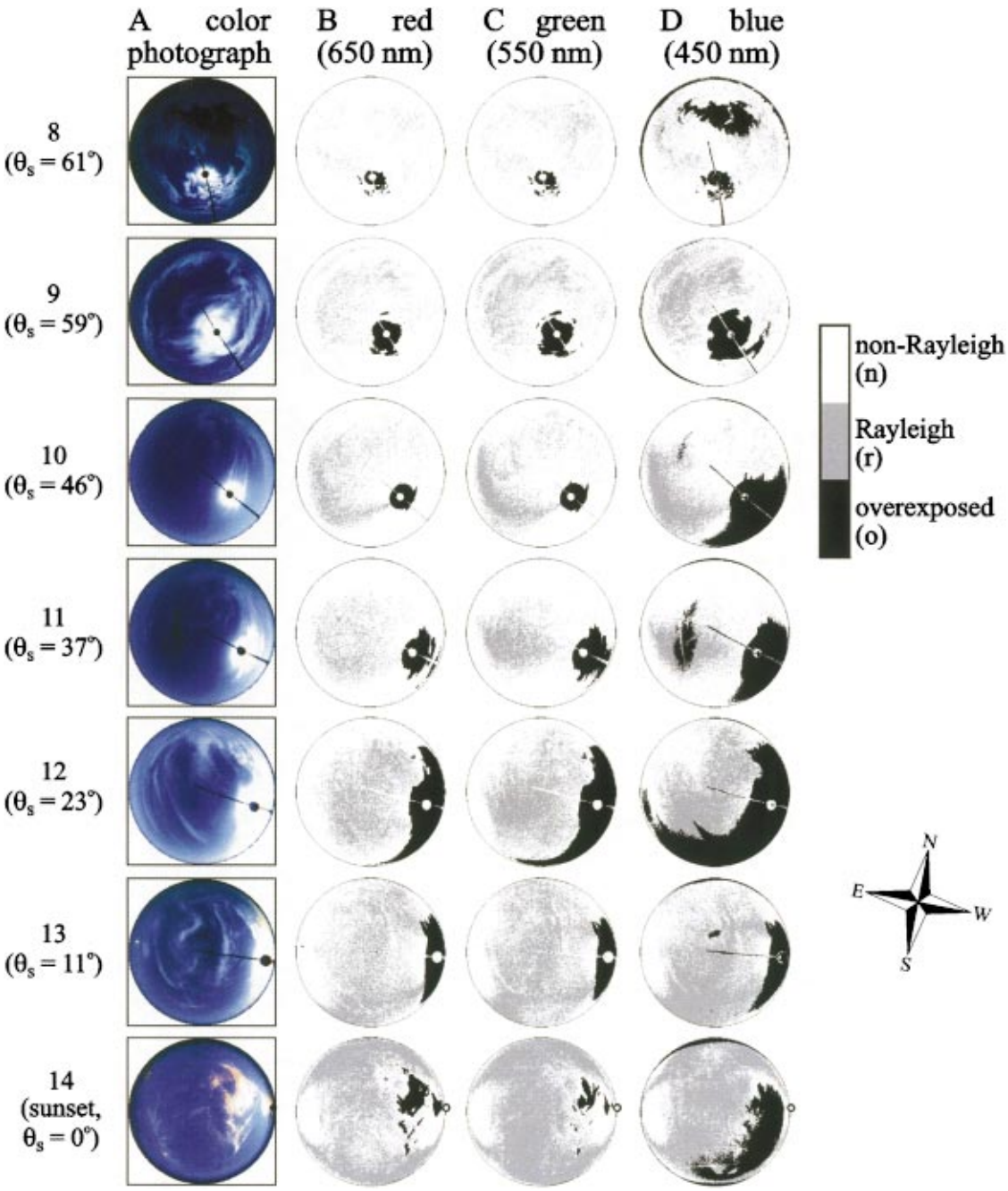

Fig. 2 (continued).

maps of Rayleigh behavior (Figs. 1 and 2 and Tables 1–3 below) and to filter out the inevitable small amount of digital noise of the sky pictures after their digitization. For the aggregated celestial pixels the average of the α values was calculated. This pixel aggregation resulted in a reduction of N from 543 000 to 150 000.] Hence r is the proportion of the sky where α corresponds to α of the single-scattering Rayleigh sky with an accuracy of α_{thres}. In the celestial maps of Rayleigh behavior (Figs. 1 and 2), "Rayleigh" points with $\Delta\alpha \leqslant \alpha_{\text{thres}}$ are shaded by gray, "non-Rayleigh" points with $\Delta\alpha > \alpha_{\text{thres}}$ are white, and the "overexposed" points are black. We define two further quantities: $n = N_{\text{non-Rayleigh}}/N$ and $o = N_{\text{overex}}/N$, where $N_{\text{non-Rayleigh}}$ is the number of non-Rayleigh points and N_{overex} is the number of overexposed points. The relation among the quantities r, n, and o is $r + n + o = 1$.

3. RESULTS

Figures 1 A and 2 A (where A, B, C, and D indicate columns in the figures) show the maps of the total radiance of the clear and partly cloudy skies investigated. In Figs. 1 B, C, D and 2 B, C, D we see the maps of r for these skies at the wavelengths of 650 nm (red), 550 nm (green), and 450 nm (blue). In these r maps the celestial regions with $\Delta\alpha = |\alpha_{\text{meas}} - \alpha_{\text{Rayleigh}}| \leqslant 5°$ are gray, the areas with $\Delta\alpha > 5°$ are white, and the overexposed regions are black. Table 1 contains the values of r, n, and o at 650,

550, and 450 nm for the clear skies in Fig. 1. Table 2 shows the values of r_{clouds}, r_{clear}, n_{clouds}, n_{clear}, and o in the red, green, and blue spectral ranges for the clear and cloudy regions of the partly cloudy skies in Fig. 2. In Table 3 the values of $r = r_{clouds} + r_{clear}$ and $n = n_{clouds} + n_{clear}$ are seen for the partly cloudy skies in Fig. 2 at 650, 550, and 450 nm. Analyzing the figures and the tables, we can establish the following trends:

1. At a given solar position and in a given spectral range, r is always higher for the clear sky than for the cloudy sky. In the clear sky (Table 1) r ranges from ≈13% to 69%, and from ≈4% to 69% in the cloudy sky (Table 3). However, when the sun is at or near the horizon and is not occluded by clouds (rows 1 and 12–14 in Figs. 1 and 2 and Tables 1 and 3), the r values of cloudy skies approximate those of clear skies.

2. The lower the solar elevation angle θ_s, the higher is r for both the clear and cloudy sky series, independently of the spectral range. Under clear sky conditions in the red part of the spectrum (where the overexposure o is the lowest, i.e., the accuracy of the measured r value is the highest), r increases from ≈19% to 65% (Table 1) as θ_s decreases from 65° (noon) to 0° (sunrise or sunset). Under cloudy sky conditions in the red, r increases from ≈4% to 56–65% (Table 3) as θ_s decreases from its highest value to zero.

Table 1. Values of r, n, and o for the Clear Skies in Fig. 1[a]

		650 nm (Red)			550 nm (Green)			450 nm (Blue)		
R	θ_s	r	n	o	r	n	o	r	n	o
1	0°	65.74	55.75	4.97	67.78	28.83	3.39	**49.94**	**36.43**	**13.63**
2	9°	59.01	28.39	12.60	**56.15**	**21.08**	**22.77**	**25.99**	**26.63**	**47.39**
3	21°	38.17	52.31	9.52	51.83	35.03	13.14	**37.44**	**35.01**	**27.55**
4	35°	25.88	62.43	11.68	35.88	46.22	17.89	**29.25**	**31.18**	**39.57**
5	45°	24.86	73.22	1.91	34.95	62.68	2.37	**34.20**	**58.33**	**7.47**
6	57°	19.94	78.04	2.02	30.25	67.41	2.34	**27.92**	**67.61**	**4.46**
7	65°	19.45	78.49	2.06	37.04	60.60	2.36	43.15	52.59	4.25
8	64°	20.09	77.78	2.13	38.63	59.09	2.29	51.59	43.60	4.81
9	58°	19.64	77.81	2.55	33.01	64.23	2.76	43.20	38.11	18.69
10	44°	18.74	77.90	3.35	37.80	58.53	3.67	43.13	40.51	16.36
11	34°	27.08	67.04	5.87	37.24	55.29	7.47	40.55	41.95	17.51
12	25°	36.88	47.93	15.20	43.60	36.12	20.28	**23.87**	**35.02**	**41.11**
13	13°	39.28	42.64	18.08	43.76	31.72	24.52	**12.53**	**35.32**	**52.15**
14	0°	64.53	32.54	2.93	69.17	28.98	1.85	**24.92**	**53.34**	**21.74**

[a] r is the proportion (%) of the sky that follows the Rayleigh model with an accuracy of $\Delta\alpha = |\alpha_{meas} - \alpha_{Rayleigh}| = 5°$; n is the proportion (%) of the sky that does not follow the Rayleigh model, o is the overexposed proportion (%) of the sky at 650 nm (red), 550 nm (green), and 450 nm (blue); R is the row number in Fig. 1; θ_s is the solar elevation angle measured from the horizon; $r + n + o = 100\%$; r, n and o values are bold for which the trend $r_{blue} > r_{green} > r_{red}$ is not satisfied.

Table 2. Values (%) of r_{clouds}, r_{clear}, n_{clouds}, n_{clear} and o at 650 nm (Red), 550 nm (Green), and 450 nm (Blue) for the Cloudy and Clear Regions of the Partly Cloudy Skies in Fig. 2.[a]

		650 nm (Red)					550 nm (Green)					450 nm (Blue)				
		Clouds		Clear			Clouds		Clear			Clouds		Clear		
R	θ_s	r_{clouds}	n_{clouds}	r_{clear}	n_{clear}	o	r_{clouds}	n_{clouds}	r_{clear}	n_{clear}	o	r_{clouds}	n_{clouds}	r_{clear}	n_{clear}	o
1	0°	32.41	23.33	32.18	11.48	0.60	34.47	21.34	33.58	10.55	0.06	20.20	23.37	8.69	10.83	36.92
2	9°	19.89	56.32	2.65	11.56	9.58	19.77	57.07	3.01	11.52	8.63	22.78	49.49	3.57	7.69	16.47
3	26°	6.77	35.11	7.95	45.32	4.85	9.50	31.71	11.96	41.29	5.55	8.24	25.40	11.80	34.72	19.84
4	34°	1.51	19.13	13.07	62.32	3.96	2.07	18.01	18.68	56.71	4.53	1.57	13.84	14.75	46.40	23.45
5	40°	1.64	20.23	13.10	61.16	3.87	3.21	18.23	22.79	51.46	4.32	1.10	15.63	20.02	45.34	17.92
6	56°	3.83	68.34	2.39	24.32	1.12	5.95	66.22	3.26	23.44	1.12	5.25	53.80	1.67	9.47	29.81
7	60°	0.46	39.30	3.50	52.95	3.79	1.03	38.30	5.85	50.81	4.02	3.03	34.84	8.87	45.68	7.58
8	61°	2.35	56.93	2.95	36.28	1.50	4.99	54.10	4.88	34.36	1.67	6.48	43.42	7.73	27.86	14.52
9	59°	1.46	28.23	9.53	56.55	4.23	3.23	25.17	16.95	49.13	5.52	4.61	18.87	23.03	41.83	11.67
10	46°	0.33	17.39	18.62	60.63	3.03	0.65	16.67	22.55	56.79	3.34	0.68	10.17	24.77	45.67	18.71
11	37°	0.29	17.18	15.31	61.51	5.72	0.43	15.46	18.32	58.59	7.20	0.32	10.27	17.63	52.38	19.41
12	23°	1.84	17.28	28.35	38.71	13.82	3.40	12.50	34.23	32.67	17.2	4.44	7.67	30.76	21.46	35.68
13	11°	7.24	16.46	34.26	35.36	6.69	8.53	15.56	42.21	27.45	6.25	8.45	13.87	44.02	24.07	9.58
14	0°	8.72	14.61	47.70	23.02	5.96	12.28	14.10	56.44	14.55	2.63	10.90	8.01	46.46	14.18	20.45

[a] R is the row number in Fig. 2, θ_s is the solar elevation angle measured from the horizon, and $r_{clouds} + r_{clear} + n_{clouds} + n_{clear} + o = 100\%$.

Table 3. Values (%) of $r=r_{\text{clouds}}+r_{\text{clear}}$, $n=n_{\text{clouds}}+n_{\text{clear}}$, and o at 650 nm (Red), 550 nm (Green), and 450 nm (Blue) for the Partly Cloudy Skies in Fig. 2[a]

		650 nm (Red)			550 nm (Green)			450 nm (Blue)		
R	θ_s	r	n	o	r	n	o	r	n	o
1	0°	64.59	34.81	0.60	68.05	31.89	0.06	**28.88**	**34.20**	**36.92**
2	9°	22.54	67.88	9.58	22.78	68.59	8.63	26.35	57.19	16.47
3	26°	14.72	80.43	4.85	21.46	72.99	5.55	**20.04**	**60.12**	**19.84**
4	34°	14.58	81.46	3.96	20.75	74.73	4.53	**16.32**	**60.23**	**23.45**
5	40°	14.74	81.38	3.87	26.00	69.69	4.32	**21.12**	**60.97**	**17.92**
6	56°	6.22	92.67	1.12	9.21	89.67	1.12	**6.91**	**63.27**	**29.81**
7	60°	3.96	92.25	3.79	6.88	89.11	4.02	11.89	80.53	7.58
8	61°	5.30	93.21	1.50	9.87	88.46	1.67	14.20	71.28	14.52
9	59°	10.99	84.78	4.23	20.17	74.30	5.52	27.63	60.70	11.67
10	46°	18.95	78.02	3.03	23.20	73.46	3.34	25.45	55.84	18.71
11	37°	15.60	78.68	5.72	18.75	74.05	7.20	**17.95**	**62.65**	**19.41**
12	23°	30.19	55.99	13.82	37.63	45.17	17.20	**35.20**	**29.13**	**35.68**
13	11°	41.49	51.82	6.69	50.74	43.01	6.25	52.47	37.95	9.58
14	0°	56.42	37.63	5.96	68.72	28.65	2.63	**57.36**	**22.20**	**20.45**

[a] R is the row number in Fig. 2, θ_s is the solar elevation angle measured from the horizon, $r + n + o = 100\%$; r, n and o values are bold for which the trend $r_{\text{blue}} > r_{\text{green}} > r_{\text{red}}$ is not satisfied.

3. For high solar elevations, r is highest in the blue part of the spectrum, lower in the green, and lowest in the red under clear as well as cloudy sky conditions (Tables 1 and 3). For lower solar elevations $r_{\text{green}} > r_{\text{red}}$, but $r_{\text{blue}} < r_{\text{green}}$.

4. Sometimes, a considerable part (r_{clouds}) of the E-vector pattern of the cloudy sky regions follows the Rayleigh pattern (Table 2). The lower the solar elevation θ_s, the higher the value of r_{clouds}, independently of the spectral range. Under cloudy sky conditions in the green, for example, r_{clouds} increases from ≈1% to 12–34% (Table 2) as θ_s decreases from its highest value to zero.

4. DISCUSSION

In the maps of Rayleigh behavior (Figs. 1 and 2) the celestial regions near the sun are more or less overexposed. As a result of the law of Rayleigh scattering, the overexposure o is the highest in the blue part of the spectrum and lowest in the red (Tables 1–3). In these overexposed sky regions the proportion r of the sky that follows the Rayleigh model is unknown. Thus as a first approximation the inaccuracy of r is o, which is lower the longer the wavelength. However, between the Babinet and Brewster neutral points around the sun the E-vector pattern differs considerably from the Rayleigh pattern because of the negative polarization.[1,29,35] Hence the overexposed areas around the sun in Figs. 1 and 2 approximately overlap the regions of negative polarization. Consequently, if the E-vector directions in the overexposed sky regions were known, these regions would contribute mainly to the value of n rather than to the r value.

Note that in Tables 1 and 3 the condition $r_{\text{blue}} > r_{\text{green}} > r_{\text{red}}$ at a given solar elevation angle θ_s (see trend 3) is usually satisfied, especially when the overexposure o is low. This atmospheric optical phenomenon partly explains why the celestial polarization pattern is detected in the UV or blue part of the spectrum by the majority of polarization-sensitive animals that orient by means of the celestial polarization pattern. The question "Why is it advantageous to perceive the polarization of skylight under cloudy conditions in the UV or blue" is answered in detail by Horváth and Varjú[1] as well as by Barta and Horváth.[2]

According to trend 1, the proportion r of the sky that follows the Rayleigh model is higher for the clear sky than for the cloudy sky at the same solar position and in a given spectral range. The reason for this is that depending on the cloud cover, the clouds more or less disturb the E-vector pattern characteristic of the clear sky. However, Brines and Gould[28] as well as Pomozi *et al.*[34] showed that the clear sky angle of polarization pattern more or less continues underneath clouds (see r_{clouds} in Table 2) if parts of the clouds and/or the air layers beneath them are lit by direct sunlight. This is the reason for trend 4. The lower the solar elevation θ_s, the higher the chance that some parts of the clouds and/or the air layers beneath them are directly lit by the sun, which explains trend 2. This chance is highest when the sun is at the horizon and is not hidden by clouds, which explains why r for cloudy skies approximates that for clear skies at sunrise and sunset if the sun is visible.

We used $\Delta\alpha = |\alpha_{\text{meas}} - \alpha_{\text{Rayleigh}}| = \alpha_{\text{thres}} = 5°$ rather arbitrarily during the calculation of the celestial Rayleigh behavior. We performed our calculations with several other threshold values; however, we found that the increase or decrease of α_{thres} increased or decreased the r value but did not influence the validity of trends 1–4 listed above.

5. CONCLUSION

We conclude that depending on the solar elevation angle θ_s, the proportion r of the sky that follows the Rayleigh model is high for clear skies, especially for low solar elevations ($40\% < r < 70\%$ for $\theta_s \leqslant 13°$). Depending on

the cloud cover and the solar illumination, r decreases more or less under cloudy conditions, but sometimes its value remains remarkably high, especially at low solar elevations ($r_{max} = 69\%$ for $\theta_s = 0°$). The proportion r is higher for shorter wavelengths under clear as well as cloudy sky conditions. This partly explains why the shorter (ultraviolet and blue) wavelengths are usually preferred by animals navigating on the basis of the celestial polarization pattern. The celestial E-vector pattern generally follows the Rayleigh pattern well, which is a fundamental hypothesis in the studies of animal orientation and human navigation (e.g., in aircraft flying near the geomagnetic poles and using a polarization sky compass) with the use of the celestial pattern of the angle of polarization.

ACKNOWLEDGMENTS

This work was supported by a 3-year István Széchenyi research fellowship from the Hungarian Ministry of Education to Gábor Horváth. We give many thanks for the valuable comments of two anonymous referees.

Corresponding author Gábor Horváth's e-mail address is gh@arago.elte.hu.

REFERENCES

1. G. Horváth and D. Varjú, *Polarized Light in Animal Vision—Polarization Patterns in Nature* (Springer, Berlin, 2003).
2. A. Barta and G. Horváth, "Why is it advantageous to perceive the polarization of downwelling light under clouds and canopies in the UV?" J. Theor. Biol. **226**, 429–437 (2004).
3. K. Kirschfeld, M. Lindauer, and H. Martin, "Problems of menotactic orientation according to polarized light of the sky," Z. Naturforsch. **30c**, 88–90 (1975).
4. R. Wehner, "Polarized-light navigation by insects," Sci. Am. **235**(7), 106–115 (1976).
5. H. W. van der Glas, "Models for unambiguous E-vector navigation in the bee," J. Comp. Physiol. A **113**, 129–159 (1977).
6. S. Rossel, R. Wehner, and M. Lindauer, "E-vector orientation in bees," J. Comp. Physiol., A **125**, 1–12 (1978).
7. M. L. Brines, "Dynamic patterns of skylight polarization as clock and compass," J. Theor. Biol. **86**, 507–512 (1980).
8. K. P. Able, "Skylight polarization patterns at dusk influence migratory orientation in birds," Nature **299**, 550–551 (1982).
9. J. B. Phillips and J. A. Waldvogel, "Reflected light cues generate the short-term deflector-loft effect," in *Avian Navigation*, F. Papi and H. G. Wallraff, eds. (Springer, Heidelberg, Germany, 1982), pp. 190–202.
10. S. Rossel and R. Wehner, "The bee's map of the E-vector pattern in the sky," Proc. Natl. Acad. Sci. USA **79**, 4451–4455 (1982).
11. R. Wehner, "Celestial and terrestrial navigation: human strategies—insect strategies," in *Neuroethology and Behavioral Physiology*, F. Huber and H. Markl, eds. (Springer, Heidelberg, Germany, 1983), pp. 366–381.
12. R. Wehner, "Astronavigation in insects," Annu. Rev. Entomol. **29**, 277–298 (1984).
13. R. Wehner and S. Rossel, "The bee's celestial compass—a case study in behavioral neurobiology," Fortschr. Zool. **31**, 11–53 (1985).
14. R. Wehner, "The hymenopteran skylight compass: matched filtering and parallel coding," J. Exp. Biol. **146**, 63–85 (1989).
15. K. P. Able and M. A. Able, "Ontogeny of migratory orientation in the savannah sparrow, Passerculus sandwichensis: mechanisms at sunset," Anim. Behav. **39**, 1189–1198 (1990).
16. K. Schmidt-Koenig, J. U. Ganzhorn, and R. Ranvaud, "The sun compass," in *Orientation in Birds*, P. Berthold, ed. (Birkhäuser, Basel, 1991), pp. 1–15.
17. C. W. Hawryshyn, "Polarization vision in fish," Am. Sci. **80**, 164–175 (1992).
18. R. Wehner, "The polarization-vision project: championing organismic biology," Fortschr. Zool. **39**, 103–143 (1994).
19. R. Wehner, "The ant's celestial compass system: spectral and polarization channels," in *Orientation and Communication in Arthropods*, M. Lehrer, ed. (Birkhäuser, Basel, 1997), pp. 145–185.
20. N. Shashar, T. W. Cronin, L. B. Wolff, and M. A. Condon, "The polarization of light in a tropical rain forest," Biotropica **30**, 275–285 (1998).
21. T. Labhart and E. P. Meyer, "Detectors for polarized skylight in insects: a survey of ommatidial specializations in the dorsal rim area of the compound eye," Microsc. Res. Tech. **47**, 368–379 (1999).
22. M. J. Freake, "Evidence for orientation using the E-vector direction of polarized light in the sleepy lizard Tiliqua rugosa," J. Exp. Biol. **202**, 1159–1166 (1999).
23. K. von Frisch, *The Dance Language and Orientation of Bees* (Harvard U. Press, Cambridge, Mass., 1967).
24. T. Ramskou, "Solstenen," Skalk **2**, 16–17 (1967).
25. T. Ramskou, *Solstenen—Primitiv Navigation I Norden for Kompasset* (Rhodos, Copenhagen, 1969).
26. W. Britton, "The Britton Viking sun-stone expedition," Nutr. Today, May/June 1972, pp. 14–23.
27. B. E. Schaefer, "Vikings and polarization sundials," Sky Telesc. **1997**(5), 91–94.
28. M. L. Brines and J. L. Gould, "Skylight polarization patterns and animal orientation," J. Exp. Biol. **96**, 69–91 (1982).
29. K. L. Coulson, *Polarization and Intensity of Light in the Atmosphere* (A. Deepak, Hampton, Va., 1988).
30. J. A. North and M. J. Duggin, "Stokes vector imaging of the polarized sky-dome," Appl. Opt. **36**, 723–730 (1997).
31. K. J. Voss and Y. Liu, "Polarized radiance distribution measurements of skylight. I. System description and characterization," Appl. Opt. **36**, 6083–6094 (1997).
32. J. Gál, G. Horváth, V. B. Meyer-Rochow, and R. Wehner, "Polarization patterns of the summer sky and its neutral points measured by full-sky imaging polarimetry in Finnish Lapland north of the Arctic Circle," Proc. R. Soc. London Ser. A **457**, 1385–1399 (2001).
33. G. Horváth, A. Barta, J. Gál, B. Suhai, and O. Haiman, "Ground-based full-sky imaging polarimetry of rapidly changing skies and its use for polarimetric cloud detection," Appl. Opt. **41**, 543–559 (2002).
34. I. Pomozi, G. Horváth, and R. Wehner, "How the clear-sky angle of polarization pattern continues underneath clouds: full-sky measurements and implications for animal orientation," J. Exp. Biol. **204**, 2933–2942 (2001).
35. G. P. Können, *Polarized Light in Nature* (Cambridge U. Press, Cambridge, UK, 1985).